JOURNAL OF SYNCHROTRON RADIATION
ISSN 1600-5775

# Effects of soft X-ray radiation damage on paraffin-embedded rat tissues supported on ultralene: a chemical perspective

Diana E. Bedolla,[a]* Andrea Mantuano,[b,c] Arissa Pickler,[d] Carla Lemos Mota,[c,d] Delson Braz,[d] Camila Salata,[e] Carlos Eduardo Almeida,[c] Giovanni Birarda,[a] Lisa Vaccari,[a] Regina Cély Barroso[b] and Alessandra Gianoncelli[a]*

[a]Elettra-Sincrotrone Trieste SCpA, SS 14, km 163,5, Basovizza, Trieste, TS 34149, Italy, [b]Physics Institute, State University of Rio de Janeiro (UERJ), Rua São Francisco Xavier 524 PJLF sala 3007F, Rio de Janeiro, RJ 20550-900, Brazil, [c]Radiological Sciences Laboratory, State University of Rio de Janeiro (UERJ), Rua São Francisco Xavier 524 PHLC Sala 136, Rio de Janeiro, RJ 20550-900, Brazil, [d]COPPE, Federal University of Rio de Janeiro, Av. Horácio Macedo 2030, Bloco G – Sala 206 – CT, Rio de Janeiro, RJ 21941-594, Brazil, and [e]Medical Physics Department, Comissão Nacional de Energia Nuclear, Rua General Severiano 90, Rio de Janeiro, RJ 22290-901, Brazil. *Correspondence e-mail: diana.bedolla@elettra.eu, alessandra.gianoncelli@elettra.eu

Received 22 December 2017
Accepted 24 February 2018

Edited by M. Yamamoto, RIKEN SPring-8 Center, Japan

**Keywords:** soft X-ray microscopy; radiation damage; Fourier transform infrared (FTIR); paraffin; ultralene; fixation.

**Supporting information**: this article has supporting information at journals.iucr.org/s

Radiation damage is an important aspect to be considered when analysing biological samples with X-ray techniques as it can induce chemical and structural changes in the specimens. This work aims to provide new insights into the soft X-ray induced radiation damage of the complete sample, including not only the biological tissue itself but also the substrate and embedding medium, and the tissue fixation procedure. Sample preparation and handling involves an unavoidable interaction with the sample matrix and could play an important role in the radiation-damage mechanism. To understand the influence of sample preparation and handling on radiation damage, the effects of soft X-ray exposure at different doses on ultralene, paraffin and on paraffin-embedded rat tissues were studied using Fourier-transform infrared (FTIR) microspectroscopy and X-ray microscopy. Tissues were preserved with three different commonly used fixatives: formalin, glutaraldehyde and Karnovsky. FTIR results showed that ultralene and paraffin undergo a dose-dependent degradation of their vibrational profiles, consistent with radiation-induced oxidative damage. In addition, formalin fixative has been shown to improve the preservation of the secondary structure of proteins in tissues compared with both glutaraldehyde and Karnovsky fixation. However, conclusive considerations cannot be drawn on the optimal fixation protocol because of the interference introduced by both substrate and embedding medium in the spectral regions specific to tissue lipids, nucleic acids and carbohydrates. Notably, despite the detected alterations affecting the chemical architecture of the sample as a whole, composed of tissue, substrate and embedding medium, the structural morphology of the tissues at the micrometre scale is essentially preserved even at the highest exposure dose.

## 1. Introduction

X-ray microscopy (XRM) has progressed rapidly in recent decades, thanks to the use of highly brilliant light sources, with the fabrication of optical elements allowing X-rays to be focused down to the nanometric scale and with recent developments in the detector field. Nowadays, different types of X-ray microscopes find applications in almost all fields, from medicine and life sciences to geochemistry, environmental and material science. In particular, soft X-ray microscopy is becoming a widespread technique for investigating biological samples at the cellular and sub-cellular level with higher spatial resolution than light microscopy, and higher penetra-

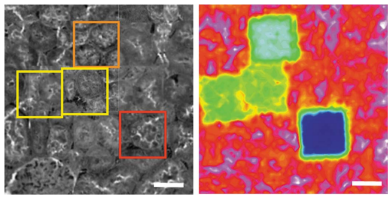

tion depth and chemical sensitivity than electron microscopy (Kaulich *et al.*, 2011). However, there are some specific aspects to be considered when working with soft X-rays. Firstly, soft X-rays typically necessitate vacuum environments and therefore suitable sample preparation is required. Secondly, soft X-rays are known to cause more damage than hard X-rays because of their increased absorption by the biological matrix and increased ionizing power (Howells *et al.*, 2009) causing chemical changes in the specimen and promoting the formation of radical species (Gianoncelli *et al.*, 2015).

Cellular component molecules can be ionized by X-rays that directly induce breaking of the molecular chemical bonds and that indirectly promote the formation of water-derived radicals that react with nearby molecules and induce the breaking of chemical bonds. Radiation-induced damage can manifest as a variation in mass density, as a reorganization of the fine morphological features of the sample, and eventually as mass translocation and possibly elemental re-distribution, especially in hydrated samples (Sayre *et al.*, 1977; Schneider, 1998; Jones *et al.*, 2017). The extent of the radiation damage depends on different factors, such as X-ray wavelength, exposure dose, sample preparation and environment.

Photoelectrons generated by the interaction of the incident photons with the sample are a potential source of X-ray induced damage (Sanishvili *et al.*, 2011). The energy deposited by the photoelectrons in the specimen depends on the composition and size of the interaction volume, suggesting that sample volume and matrix is a key factor in the radiation-damage process. Adding chemical compounds that block or reduce the radiation damage process during X-ray diffraction and X-ray crystallography measurements dates back to the 1970s (Sarma & Zaloga, 1975). Further studies in this field have shown that some antioxidants and free-radical scavengers can provide protection and increase lifetimes for protein crystals during synchrotron irradiation (Massover, 2007; Murray & Garman, 2002; Kauffmann *et al.*, 2006).

Recently, the damaging effect of soft X-rays was investigated on formalin fixed cells by means of two additional independent non-destructive microscopy methods: atomic force microscopy (AFM) and Fourier transform infrared microspectroscopy (FTIRM) (Gianoncelli *et al.*, 2015). The results showed that the ionizing radiation damages the formalin fixed cells by inducing extensive oligomerization of bio-macromolecules that results in complete disintegration of the vibrational architecture (Gianoncelli *et al.*, 2015).

This paper builds on previous work in this area (Gianoncelli *et al.*, 2015) moving from single cells to investigating the effect of soft X-ray induced damage on paraffin-embedded kidney and liver rat tissues prepared with three different fixation protocols. Biological tissues exhibit a more complex hierarchical structure than single cells architecture leading to a more complex radiation damage process. Moreover, tissues usually require infiltration of an embedding material to allow thin sections to be cut for analysis, further complicating the specimen matrix and therefore its reaction to X-ray exposure. Paraffin was used as the embedding material in this study as it is one of the most common protocols for tissue sectioning for visible-light microscopy studies and is often used for X-ray microscopy investigations.

In the present study, radiation damage was induced through XRM measurements to detect structural changes and FTIRM to detect possible chemical changes. As FTIRM is a label-free and non-destructive technique that probes matter by using low-energy photons (0.05–0.5 eV), it does not induce any further possible specimen damage, thus the observed chemical changes can be safely attributed to X-rays alone.

The information derived from this study will provide the soft X-ray microscopy community with a better understanding of the influence of fixation protocol on radiation damage in paraffin-embedded tissue sections. We find that formalin fixation is more resistant to radiation damage than both glutaraldehyde and Karnovsky fixation while significant radiation-induced damage is observed in both paraffin and ultralene.

## 2. Materials and methods

### 2.1. Sample preparation

The animals used were three isogenic three-months-old Wistar rats obtained from the Radiological Sciences Laboratory of the State University of Rio de Janeiro, Brazil. The animals were kept in an appropriate environment on a 12 h light/dark cycle with free access to food and water, maintained under standard animal facility conditions. The animals were not subject to any type of special treatment. All procedures were carried out according to international guidelines of animal protection. One kidney and the liver of each rat were removed, cleaned and immersed in a fixative. A different fixative was used for the tissues of each rat. The fixatives used were as follows: 10% neutral buffered formalin (4% formaldehyde) (F), 2.5% glutaraldehyde in 0.1 *M* sodium cacodylate buffer, pH 7.2 (G) and Karnovsky (2.5% glutaraldehyde, 4% paraformaldehyde in 0.1 *M* sodium cacodylate buffer, pH 7.2) (K). After fixation, tissues were embedded in paraffin and the liver and kidney tissues were sectioned to 5 µm-thick slices and deposited on 4 µm-thick ultralene foils (SPEX SamplePrep, LLC) for X-ray analyses.

The study was approved by the ethic boards of the Radiological Sciences Laboratory of the State University of Rio de Janeiro, and the methods were carried out according to the committee that approved the experimental protocols (No. CEA/010/2012).

### 2.2. Soft X-rays exposure

The tissues were analysed at the TwinMic soft X-ray microscopy beamline (Gianoncelli *et al.*, 2016; Kaulich *et al.*, 2006) (Elettra Sincrotrone Trieste, Trieste, Italy) and exposed to different radiation doses. For this experiment, TwinMic operated in scanning mode, where the sample is raster-scanned under a microprobe delivered by a zone plate (ZP) diffractive optic. A fast-readout CCD camera located downstream of the sample produces absorption and phase contrast images, providing morphological information on the scanned

Table 1
Summary of the exposed areas in fixed-embedded tissue on ultralene, paraffin on ultralene and pristine ultralene that are depicted in Fig. 3.

ID represents the increasing dose that the different areas were subjected to.

| ID | Tissue exposed area (μm) | Paraffin exposed area (μm) | Ultralene exposed area (μm) | Radiation dose (Gy) |
|---|---|---|---|---|
| Rad1 | 400 × 400 | 240 × 240 | 240 × 240 | $1.67 \times 10^6$ |
| Rad2 (yellow) | 80 × 160 | 80 × 160 | 80 × 160 | $1.83 \times 10^7$ |
| Rad3 (orange) | 80 × 80 | 25 × 25 | 25 × 25 | $1.43 \times 10^8$ |
| Rad4 (red) | 80 × 80 | 25 × 25 | 25 × 25 | $1.02 \times 10^9$ |

areas (Gianoncelli *et al.*, 2006; Morrison *et al.*, 2006). At the same time X-ray fluorescence spectra can be collected by eight silicon drift detectors (SDDs) placed in front of the sample, providing the elemental distribution of the excited chemical elements (Gianoncelli *et al.*, 2009, 2013). For these measurements, an incident photon energy of 1.5 keV and a 600 μm-diameter Au ZP with an outermost zone of 50 nm were used, producing a spot size of 1 μm in diameter, a typical experimental setup for biological tissue analyses at TwinMic (Mitri *et al.*, 2017).

Owing to the relative homogeneity of the tissues, separate areas were exposed to different radiation doses. Each sample was exposed to areas of increasing radiation dose (Rad1, Rad2, Rad3 and Rad4) as outlined in Table 1. The different radiation doses were obtained by increasing the dwell time per pixel used in the scanning. Areas of the same slice with paraffin only and with pristine ultralene foil were exposed following the same protocol for each corresponding tissue sample.

### 2.3. FTIRM measurements

Once exposed and analysed at TwinMic, the tissues were transferred to the synchotron infrared source for spectroscopy and imaging (SISSI) beamline (Lupi *et al.*, 2007) (Elettra Sincrotrone Trieste, Trieste, Italy), where the areas exposed to soft X-rays were investigated with FTIRM using a Hyperion 3000 Vis–IR microscope coupled with a Bruker Vertex 70v interferometer equipped with a 64 × 64 pixels liquid-nitrogen-cooled bi-dimensional focal plane array (FPA) detector using a globar source. For each sample, hyperspectral images were acquired in transmission mode using a 15× condenser/objective, achieving a pixel resolution of ∼2.6 μm. The areas exposed to X-rays were identified and imaged. Some unexposed regions of the same samples were also mapped and used as a control reference, named here as Rad0 condition. Background images were acquired in air. Each image was composed of at least 4096 spectra, obtained by averaging 256 scans for each detector pixel with a spectral resolution of 4 $cm^{-1}$, with large areas as a mosaic consisting of up to 2 × 2 images. All acquisitions were corrected for spectral features related to atmospheric water-vapour and $CO_2$ contributions with the atmospheric compensation routine of *Opus* 7.1 (Bruker Optics GmbH, Germany). Before hyperspectral analysis, an offset correction was applied to all acquired spectra.

Chemical images were generated by integrating the area under the curve for different infrared regions. In particular, different spectral regions can provide helpful information on the effect of radiation damage. For instance, the asymmetric $CH_3$ band (∼2960 $cm^{-1}$) trend along the tissue provides reliable identification of different exposed areas (Rad1, Rad2, Rad3 and Rad4). Specifically, average absorbance spectra for each exposed region were obtained extracting all the corresponding spectra within the area, excluding the edges. Second derivatives were then computed using *Opus* 7.1 software in the 3800–900 $cm^{-1}$ spectral range with the Savitzky–Golay filter (13 smoothing points). In Figs. 3(*c*) and 3(*d*) (see §3.1), spectra were cut at 1180–1140 $cm^{-1}$, and baseline corrected (rubber-band method) for comparison reasons.

## 3. Results and discussion

### 3.1. Biological tissues

Firstly, tissues were analysed at the TwinMic beamline and exposed to different radiation doses through scanning transmission X-ray microscopy (STXM) and low-energy X-ray fluorescene (LEXRF) measurements, as specified above (Table 1). Areas were chosen by inspecting the tissue slices and identifying regions with specific morphology (Brown *et al.*, 2016).

As an example, in Fig. 1, X-ray transmission images of kidney tissue fixed with glutaraldehyde acquired at Rad1 dose, and images acquired to complete the Rad2, Rad3 and Rad4 conditions, were used to compare the morphology of the samples before and after irradiation. All X-ray transmission images were normalized by the incident beam intensity. It is noteworthy to mention that the cellular morphology is preserved at the micrometric length scale, even when progressively increasing the radiation dose. No lateral shrinkage is observed with XRM with increasing dose; however, a reduction in sample absorption can be detected already at Rad2, with a further decrease for Rad3 and Rad4 (Fig. 1), demonstrating that the tissue is undergoing radiation damage at Rad1 dose levels in the form of mass loss in line with results in single formalin-fixed cells (Gianoncelli *et al.*, 2015). Moreover, some bright features start appearing at Rad3 (Fig. 1): in particular, some brighter areas (very likely small voids) that indicate higher transmission become more and more evident both in brightness and size when increasing the radiation dose (Fig. 1, Rad3, Rad4), suggesting possible crack formation.

While XRM allows identification of mass loss, FTIRM was utilized to assess the effect of radiation damage on the chemical composition of the exposed specimens. Fig. 2(*a*) shows the spectra obtained on kidney tissue (Fig. S1 in the supporting information reports the same information for liver tissue) from three different fixation protocols [formalin (F), glutaraldehyde (G) and Karnovsky (K)], at the initial state (Rad0, no X-ray exposure) and exposed at four radiation doses, from Rad1 to Rad4.

Among the main characteristic bands for biological tissues are those of proteins. Amide I and II bands originate from the peptide backbone; amide I, mostly from the C═O bond of the peptide backbone, ranges from about 1700 to 1580 $cm^{-1}$; amide II, from the N–H bending and C–N stretching vibrations of the same bond, ranges from 1580 to 1480 $cm^{-1}$. Since C═O and N—H bonds are involved in the hydrogen bonds that contribute to the secondary structure of proteins, the peak location of amide I and II is sensitive to their structure. For the investigated tissues, three bands are observed and highlighted in Fig. 2(*a*): amide I peaked at ∼1652 $cm^{-1}$, amide II at ∼1536 $cm^{-1}$ and amide A at ∼3295 $cm^{-1}$, associated with the N–H stretch of proteins in resonance with amide II overtone. As shown in Figs. 2(*a*) and S1 (see supporting information), the contribution of all the aforementioned protein peaks decreases with increasing radiation dose, for kidney tissues and liver tissues, respectively. In particular, for the fixation protocols under investigation, the amide I band decreases while a broad and intense spectral contribution centred at 1710 $cm^{-1}$, possibly associated with carbonyl groups in aldehyde, ketone or carboxylic groups, increases. The intensity of the amide II band also decreases as a function of the exposure dose, but the relative height of the two bands changes, possibly due to the merging of the amide I band with the carbonyl band. Overall, a fragmentation of the peptide chains can be inferred by the trend described above, and it is in

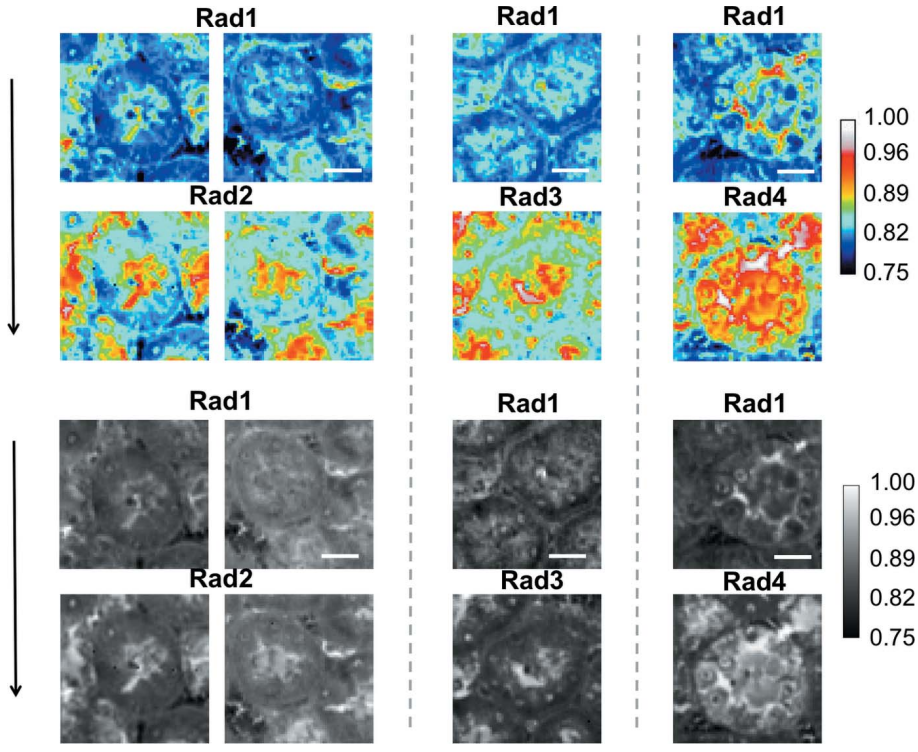


**Figure 1**
X-ray transmission images of a kidney tissue fixed with glutaraldehyde (G). All the X-ray absorption images are shown in colour and black and white to better highlight transmission values and morphology, respectively. First and third rows show the same absorption images (in different scale colour) at Rad1 radiation dose. Second and fourth rows show the same areas at further radiation doses (Rad2, Rad3 and Rad4 as specifically indicated). The scale bars represent 20 µm.

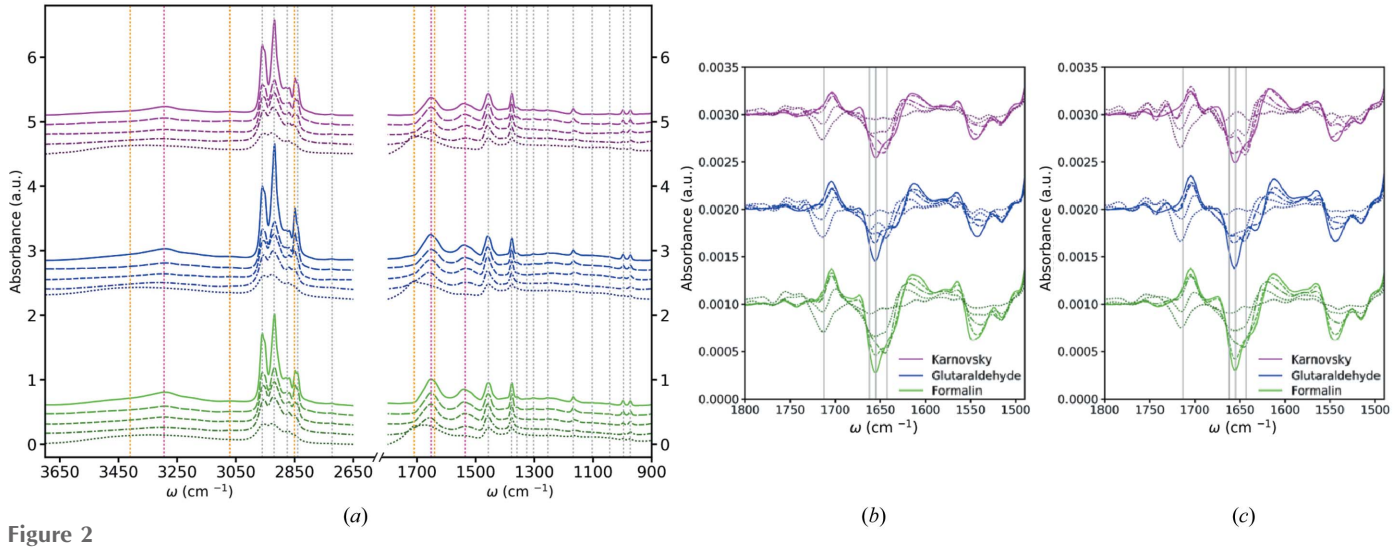


**Figure 2**
(*a*) Dose dependent FTIR absorbance spectra of a region of kidney tissues with different fixation protocols: green (bottom), formalin; blue (middle), glutaraldehyde; violet (top), Karnovsky. Radiation doses go from continuous line Rad0 to progressively dotted line Rad4. Spectral groups are displayed with an offset for clarity (in arbitary units). Grey lines refer to components from the ultralene (2960, 2920, 2870, 2839, 2722, 1457, 1378, 1359, 1326, 1303, 1254, 1168, 1103, 1043, 996, 973 $cm^{-1}$), orange lines mark components derived from paraffin on ultralene (3071, 2851, 1710, 1640 $cm^{-1}$) and fuchsia lines mark the components from the tissues (3295, 1652, 1536 $cm^{-1}$). (*b*, *c*) Second derivatives of the studied tissues with the different fixation protocols, liver and kidneys, respectively. Grey lines refer to the bands at 1713, 1662, 1655 and 1643 $cm^{-1}$ (from left to right).

agreement with previous observations for the amide I band in formalin-fixed cells exposed at comparable doses (Gianoncelli *et al.*, 2015).

The well known sensitivity of amide bands, especially of amide I, to protein secondary structure allowed us to retrieve further details associated with protein conformational changes upon X-ray exposure. Figs. 2(*b*) and 2(*c*) depict the second derivatives in the amide I and II bands (spectral region: 1800–1500 $cm^{-1}$) for both types of tissues in order to highlight the changes in secondary structure of proteins. Clearly proteins are being affected by soft X-ray radiation (Figs. 2*b* and 2*c*). Analysis of the formalin-fixed results shows that the main component of amide I at Rad0 peaks at 1655 $cm^{-1}$ [associated mainly with $\alpha$-helix folded proteins (Barth, 2007)], while for the Rad2 and Rad3 radiation doses the main amide I peak is red-shifted or in some cases bifurcated to 1643 $cm^{-1}$. This trend can be associated with a relative higher content of $\beta$-sheet and random folded proteins (Barth, 2007). Up to Rad3, amide A band shows no broad feature associated with stretching modes of water. Therefore, an extensive contribution of the bending mode of water centred at about 1640 $cm^{-1}$ can be excluded by the spectral analysis. Only at Rad4 a very broad band centred at about 3510 $cm^{-1}$ appears, partially covering the amide A band at 3295 $cm^{-1}$. These broad features are associated with –OH stretching modes, possibly by water but also from alcoholic and carboxylic groups.

At the highest exposure dose, the amide I band is essentially unstructured, consistent with the hypothesis of an extensive fragmentation of the peptide backbone leading to a decrease in band intensity. The same conclusions can be drawn by considering the trend of the amide II band. At Rad0, the amide II band region shows two contributions, one at 1540 $cm^{-1}$ (typically assigned to $\alpha$-helix structures) and one at 1516 $cm^{-1}$ [$\beta$-sheet structures (Lee & Chapman, 1986)], that diminish and then disappear at Rad4. For G and K protocols, changes in protein secondary structure were already observed after the lightest exposure (Figs. 2*b* and 2*c*). It is well known that the mechanism of formaldehyde fixation occurs through the formation of cross-links between proteins, or between proteins and nucleic acids involving hydroxymethylene bridges (Helander, 1994; Werner *et al.*, 2000; French & Edsall, 1945), with proteins maintaining their secondary structure (Mason & O'Leary, 1991). However, glutaraldehyde has protein denaturing effects (Bozzola & Russell, 1999). Since both K and G fixatives contain glutaraldehyde, it is therefore expected that the tissues might be already more prone to radiation as shown in Figs. 2(*b*) and 2(*c*). Actually, when comparing the pristine state (Rad0) of the different protocols, an enhanced contribution appears for G and K at 1631 $cm^{-1}$, in agreement with the evidence that F preserves the secondary structure to a greater degree.

The spectral intensity of the symmetric and asymmetric bands of methyl and methylene (3000–2800 $cm^{-1}$ region) diminishes with radiation exposure. Therefore, the asymmetric stretching band of methyl moieties (2960 $cm^{-1}$) was used as a measure of radiation-induced damage for generating the chemical images (Figs. 3*b*, 3*d* and 3*f*). Fig. 3(*b*) confirms that aliphatic chains are affected by radiation in the tissue. However, these moieties are also the main components of ultralene and paraffin. To better understand which component of the sample is more prone to degradation by soft X-ray exposure, the complete tissue sample (Figs. 3*a* and 3*b*), paraffin (on ultralene) (Figs. 3*c* and 3*d*) and ultralene (Figs. 3*e* and 3*f*) were analysed. In each case several sub-areas were exposed, shown with coloured squares in Figs. 3(*a*) and 3(*c*) for tissues and paraffin, respectively. Fig. 3(*e*) shows how radiation damage upon exposure also appears in the optical image of pristine ultralene. Similar results were observed for all the other samples (data not shown). As for the case of tissues, the major changes between exposed and non-exposed

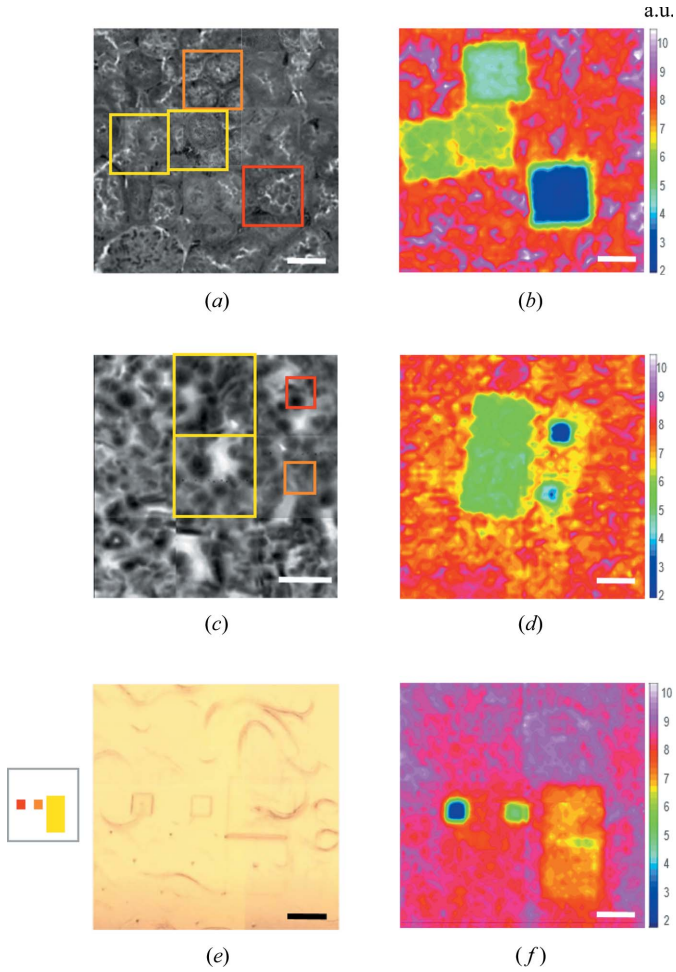


**Figure 3**
X-ray transmission images of (*a*) paraffin-embedded kidney section fixed with Karnovsky fixative supported on ultralene foil and (*c*) a paraffin-only area outside the biological tissue region, with corresponding FTIR chemical images of the integration of the absorbance of the asymmetric stretching of $CH_3$ (2960 $cm^{-1}$) band (*b* and *d*, respectively). X-ray transmission images were acquired by exposing the sample to Rad1 dose. The sample regions marked with yellow, orange and red boxes were exposed to Rad2, Rad3 and Rad4 doses, respectively. (*e*) Optical image of the exposed area on ultralene only, as indicated in the scheme in the left subset, and (*f*) its corresponding chemical image obtained by using FTIRM. FTIR chemical images are false coloured with low numbers corresponding to high damage (low signal) [colour scale bar represents absorbance arbitrary units (a.u.)]. The scale bars represent 50 µm.

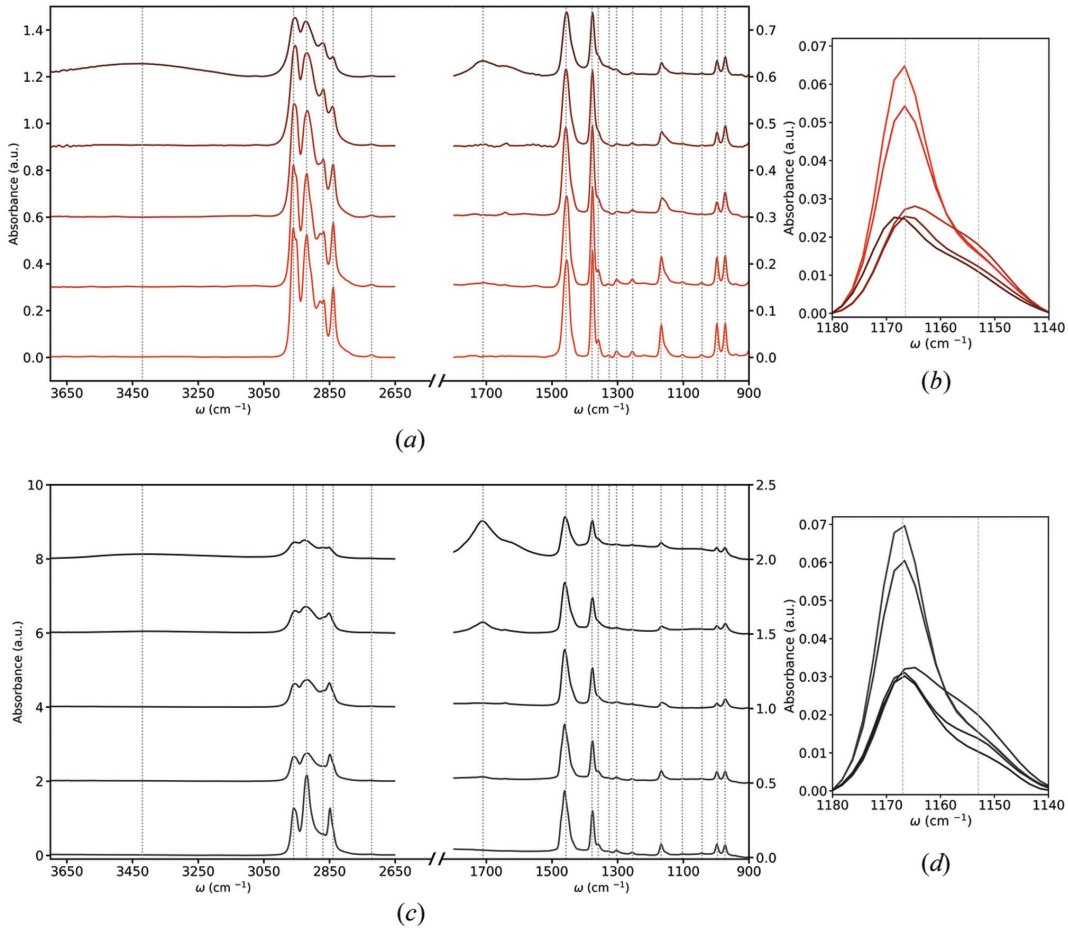


**Figure 4**
(*a*) Ultralene FTIR absorbance spectra at different exposure doses from Rad0 (lighter red colour, at the bottom) to Rad4 (darker red colour, at the top). Spectra are displayed with an offset of 0.3 a.u. (arbitary units) for clarity. Characteristic bands are highlighted with grey lines for further reference: 3420 $cm^{-1}$ (only at Rad4), 2960, 2920, 2870, 2839, 2722, 1710 (only at Rad4), 1457, 1378, 1359, 1326, 1303, 1254, 1168, 1103, 1043, 996, 973 $cm^{-1}$ (from left to right). (*b*) Close-up of the ultralene FTIR absorbance spectrum in the range 1180–1140 $cm^{-1}$. Bands highlighted with grey lines indicate the component at ∼1166 and at ∼1155 $cm^{-1}$. (*c*) Paraffin on ultralene FTIR absorbance spectra at different exposure doses from Rad0 (at the bottom) to Rad4 (at the top). Spectra are displayed with an offset of 2.0 a.u. for clarity. (*d*) Close-up of the paraffin supported on ultralene FTIR absorbance spectrum in the range 1180–1140 $cm^{-1}$.

areas lie in the spectral region corresponding to the vibration of aliphatic chains (see Fig. 4). Indeed, the contrast generated by the changes in the intensity of the 2960 $cm^{-1}$ band is quite evident (Figs. 3*b*, 3*d* and 3*f*). Chemical maps show not only the outline of the irradiated area but also the dose dependency of the complete tissue sample, paraffin (on ultralene) and ultralene. Therefore, when analysing these kinds of samples, the focus should be not only on the variations of the exposed tissue but also on the effect of the exposure on the embedding and supporting materials.

### 3.2. Ultralene

Ultralene is a polymeric film, of patented composition, typically 4 µm thick and heat resistant up to 100°C. While its transparency to soft X-rays makes it a suitable support for analysing slices of tissues or other types of samples, for mid-IR spectroscopy ultralene polymer displays a very complex spectrum. Fig. 4(*a*) shows a representative ultralene spectrum that clearly reveals the olefin-like nature of the polymer. In fact, the majority of the peaks correspond to stretching and bending modes of ═CH, $CH_2$, $CH_3$, C—C and C—O, typical of an organic compound, which, unfortunately, overlap with some of the spectral features of biological tissues. The aforementioned components are highlighted in grey in Figs. 2(*a*) and 4. In addition to the information retrieved by the chemical images in Fig. 3(*f*), the series of ultralene spectra as a function of the exposure dose shown in Fig. 4(*a*) highlight a dose-dependent decrease in the spectral intensity of the characteristic methyl and methylene bands of ultralene. Moreover, at the highest radiation dose, additional spectral contributions appear, related to —OH (∼3420 $cm^{-1}$) and C═O (∼1710 $cm^{-1}$) stretching, and possibly to the water bending mode (∼1640 $cm^{-1}$). In the region 1180–1140 $cm^{-1}$, a clear decrease in the intensity of the signal at ∼1166 $cm^{-1}$ is observed (Fig. 4*b*), which might be related to the breaking

of C=C bonds. A shoulder at ~1155 $cm^{-1}$, that could be attributed to C—O bonds of alcohols, appears after the second level of radiation exposure (Rad2), gradually diminishing and fading out with increasing radiation doses (Rad3 and Rad4). Overall, the appearance of oxydril and carbonyl bands, together with the decrease in intensity of the region 3000–2800 $cm^{-1}$, could be a consequence of the breaking of the aliphatic chains of the ultralene during irradiation, forming oxidized species, which at higher radiation conditions might eventually result in the formation of carbonyl groups, probably of aldehydic, ketonic and carboxylic nature, and promote the physisorption of some water molecules. In the study by Wasserman *et al.* (1989), the authors observed for thin layers of alkylsiloxanes a decrease in the contact angle of water after being irradiated by X-rays, which hints at an increase in hydrophilicity of the sample. Further XPS investigations supported the hypothesis of the generation of more oxidized species after measurement in air, with our findings in agreement.

### 3.3. Paraffin on ultralene

Paraffin is entirely composed of hydrocarbons, most of which are long-chain saturated compounds with no oxygen in the structure. The paraffin FTIR spectrum displays intense peaks at 720, 1380, 1466, 2847, 2910, 2953 $cm^{-1}$ (Varshney *et al.*, 2012), where the C—H bending absorption of the methyl groups at 1380 $cm^{-1}$, the C—H deformation around 1466 $cm^{-1}$, and the $CH_2$ rocking absorption band at 720 $cm^{-1}$ confirm its linear saturated aliphatic structure. In our spectra, shown in dark grey colour in Fig. 4(*c*) (and also in Fig. S2 for all acquired areas), only the band at ~2850 $cm^{-1}$ is clearly identified since the rest of the bands are actually covered by the contribution of the ultralene foil (bands highlighted in grey) present in all the following measurements as a substrate.

After exposure to X-rays at various doses, the same spectral variations highlighted for ultralene can be observed for paraffin on ultralene: at higher radiation doses, new bands centred at around ~1640 $cm^{-1}$, ~1710 $cm^{-1}$ and a large broad band centred at ~3410 $cm^{-1}$ appear. Regarding the 1180–1140 $cm^{-1}$ region, the same spectral changes observed for ultralene are also observed for paraffin on ultralene (see Fig. 4*d*).

### 3.4. Summary

Paraffin and ultralene are essentially polymeric materials, characterized by long aliphatic chains that clearly degrade as a function of the X-ray exposure dose. In order to disentangle their degradation profile, and to investigate how their spectral features interfere with the biological ones, we investigated the percentage decrease of the integral area of the aliphatic chains spectral region on ultralene (Fig. 5*a*), paraffin supported on ultralene (Fig. 5*b*), and on kidney tissue embedded on paraffin and deposited on ultralene (Fig. 5*c*) for the different radiation doses (for liver tissue see Fig. S3), normalized with respect to the initial state (Rad0).

It is quite noticeable how radiation damage can be followed in this region, due to a combined effect on tissue, paraffin and ultralene. After the lowest radiation dose (Rad1), ultralene (Fig. 5*a*) shows a slight decrease of around 10%, and a subsequent strong decrease of another 40% for higher radiation doses (Rad4). On the other hand, paraffin on ultralene (Fig. 5*b*) shows a steeper decrease (of about 40%) from Rad0 to Rad1, and a further decrease of another 20% from Rad3 to Rad4, while remaining constant for all intermediate steps. From Figs. 5(*a*) and 5(*b*) we can speculate that ultralene is less affected from Rad1 to Rad3, while paraffin shows a faster degradation already at Rad1. Liver (see Fig. S3) and kidney (Fig. 5*c*) tissues exhibit a descent of about 33% in the first step and a further descent of about 35% in the last step. This behaviour appears to be a combination of ultralene and paraffin, but a contribution of the tissue itself cannot be excluded. Tissue samples are themselves sensitive to radiation, as clearly shown by the amide I and amide II band analysis in

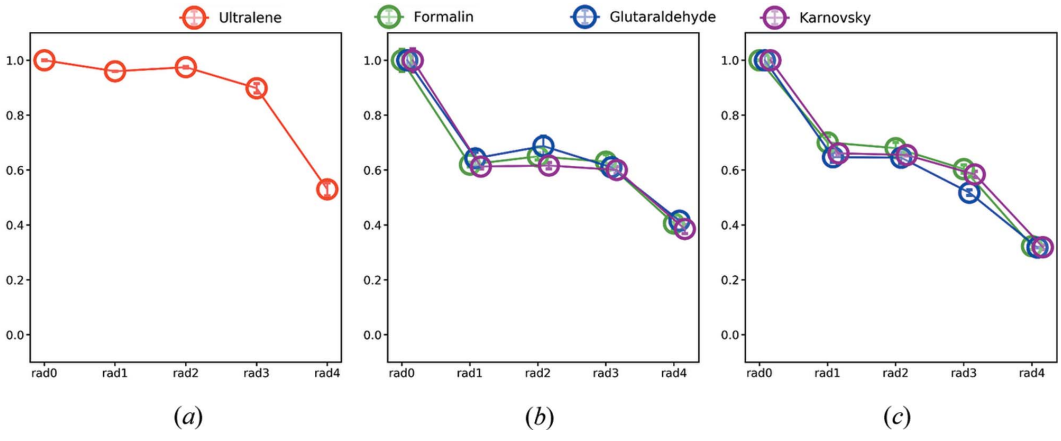


**Figure 5**
Percentage integral values with respect to the non-exposed condition for different fixation protocols for the aliphatic chains spectral region (3000–2800 $cm^{-1}$) for ultralene (*a*), paraffin on ultralene (*b*) and kidney tissue (*c*). Green: formalin; blue: glutaraldehyde; violet: Karnovsky. Data points depict the standard deviation in the *y* direction.

Figs. 2(*b*) and 2(*c*) and X-ray transmission variations shown in Fig. 1.

## 4. Conclusions

In the present study, XRM and FTIRM were used to assess the soft X-ray radiation damage of liver and kidney tissues after different fixation procedures. The tissues were embedded in paraffin and deposited on ultralene support and results were taken for paraffin only and for pristine ultralene.

In tissues, the second derivative of the FTIR spectra highlighted protein secondary structure changes induced by radiation, with changes already observed during the initial radiation dose in some fixation protocols as described in §3.1. G and K protocols show the least tolerance to soft X-ray radiation, while F protocol starts showing some degradation at higher radiation doses. Therefore, on these kinds of tissues, F protocol seems more resistant to radiation damage. Despite these clear radiation-dependent effects on the sample chemistry and the density loss, the tissue morphology seems to be preserved at micrometric length-scales in both tissues and for all fixation protocols, except for the formation of some micrometric cracks or holes and uniform mass loss, testifying that even though valid for X-ray imaging investigations, great care should be taken in case of subsequent analysis with chemical sensitive techniques.

Chemical variations detected by vibrational spectroscopy on exposed biological samples can be either related to the X-ray exposure degradation effect, or to the contributions that both substrate and embedding medium can give to the final spectral profile. Our results show that both ultralene and paraffin undergo dose-dependent radiation damage, inducing oxidation of the materials, revealed by the appearance of hydroxyl and carbonyl spectral features and by water physisorption. This suggests that the radiation damage process withstood by the specimens is more complex than in isolated biological tissues. Therefore, special care has to be devoted to the analysis of the vibrational profiles, in order to disentangle the spectral contribution of the real biological sample from the contribution of the support and embedding medium.

The next logical step will be to investigate the same tissues without using paraffin embedding. These alternative procedures will remove the strong radiation damage effect seen on paraffin and will better highlight the damage effect on the tissue. Choosing other supports, such as $Si_3N_4$ or SiC membranes, when possible, would also decouple the ultralene degradation from the tissue and paraffin degradation, and would further improve the diagnostic capabilities of FTIR microspectroscopy.

While in X-ray diffraction and X-ray crystallography fields the observations and discussion on radiation damage issues appear already quite mature (Massover, 2007), in the soft X-ray microscopy field the literature is still sparse and not comprehensive. The advent of new diffraction-limited storage rings which will produce even brighter synchrotron beams further stresses the necessity of increasing our knowledge of the X-ray radiation damage issue. Therefore, even though our results need additional investigation, they add further knowledge on the topic and should draw the attention of microscopists to the importance of the sample-embedding environment.

## Acknowledgements

We acknowledge Dr Michael W. M. Jones for careful reading of the manuscript.

## Funding information

Funding for this research was provided by: ICTP-Elettra Users Programme support to AM, AP, CLM, DB, CS, CEA, RCB.

## References

Barth, A. (2007). *Biochim. Biophys. Acta*, **1767**, 1073–1101.
Bozzola, J. J. & Russell, L. D. (1999). *Electron Microscopy: Principles and Techniques for Biologists*. Sudbury, Massachusetts: Jones and Bartlett Learning.
Brown, D. L., Staska, L. M. & Pike, J. T. (2016). *Atlas of Histology of the Juvenile Rat*, edited by G. A. Parker & C. A. Picut, pp. 173–201. Boston: Academic Press.
French, D. & Edsall, J. T. (1945). *Adv. Protein Chem.* **2**, 277–335.
Gianoncelli, A., Kaulich, B., Alberti, R., Klatka, T., Longoni, A., de Marco, A., Marcello, A. & Kiskinova, M. (2009). *Nucl. Instrum. Methods Phys. Res. A*, **608**, 195–198.
Gianoncelli, A., Kourousias, G., Merolle, L., Altissimo, M. & Bianco, A. (2016). *J. Synchrotron Rad.* **23**, 1526–1537.
Gianoncelli, A., Kourousias, G., Stolfa, A. & Kaulich, B. (2013). *J. Phys. Conf. Ser.* **425**, 182001.
Gianoncelli, A., Morrison, G. R., Kaulich, B., Bacescu, D. & Kovac, J. (2006). *Appl. Phys. Lett.* **89**, 251117.
Gianoncelli, A., Vaccari, L., Kourousias, G., Cassese, D., Bedolla, D. E., Kenig, S., Storici, P., Lazzarino, M. & Kiskinova, M. (2015). *Sci. Rep.* **5**, 10250.
Helander, K. G. (1994). *Biotech. Histochem.* **69**, 177–179.
Howells, M. R., Beetz, T., Chapman, H. N., Cui, C., Holton, J. M., Jacobsen, C. J., Kirz, J., Lima, E., Marchesini, S., Miao, H., Sayre, D., Shapiro, D. A., Spence, J. C. H. & Starodub, D. (2009). *J. Electron Spectrosc. Relat. Phenom.* **170**, 4–12.
Jones, M. W. M., Hare, D. J., James, S. A., de Jonge, M. D. & McColl, G. (2017). *Anal. Chem.* **89**, 12168–12175.
Kauffmann, B., Weiss, M. S., Lamzin, V. S. & Schmidt, A. (2006). *Structure*, **14**, 1099–1105.
Kaulich, B., Bacescu, D., Susini, J., David, C., Di Fabrizio, E., Morrison, G. R., Charalambous, P., Thieme, J., Wilhein, T., Kovac, J., Cocco, D., Salomé, M., Dhez, O., Weitkamp, T., Cabrini, S., Cojoc, D., Gianoncelli, A., Vogt, U., Podnar, M., Zangrando, M., Zacchigna, M. & Kiskinova, M. (2006). *IPAP Conf. Ser.* **7**, 22–25.
Kaulich, B., Thibault, P., Gianoncelli, A. & Kiskinova, M. (2011). *J. Phys. Condens. Matter*, **23**, 083002.
Lee, D. C. & Chapman, D. (1986). *Biosci. Rep.* **6**, 235–256.
Lupi, S., Nucara, A., Perucchi, A., Calvani, P., Ortolani, M., Quaroni, L. & Kiskinova, M. (2007). *J. Opt. Soc. Am. B*, **24**, 959–964.
Mason, J. T. & O'Leary, T. J. (1991). *J. Histochem. Cytochem.* **39**, 225–229.
Massover, W. H. (2007). *J. Synchrotron Rad.* **14**, 116–127.
Mitri, E., Millucci, L., Merolle, L., Bernardini, G., Vaccari, L., Gianoncelli, A. & Santucci, A. (2017). *Biochim. Biophys. Acta*, **1861**, 1000–1008.
Morrison, G. R., Gianoncelli, A., Kaulich, B., Bacescu, D. & Kovac, J. (2006). *IPAP Conf. Ser.* **7**, 377–379.

Murray, J. & Garman, E. (2002). *J. Synchrotron Rad.* **9**, 347–354.
Sanishvili, R., Yoder, D. W., Pothineni, S. B., Rosenbaum, G., Xu, S., Vogt, S., Stepanov, S., Makarov, O. A., Corcoran, S., Benn, R., Nagarajan, V., Smith, J. L. & Fischetti, R. F. (2011). *Proc. Natl Acad. Sci. USA*, **108**, 6127–6132.
Sarma, R. & Zaloga, G. (1975). *J. Mol. Biol.* **98**, 479–484.
Sayre, D., Kirz, J., Feder, R., Kim, D. M. & Spiller, E. (1977). *Ultramicroscopy*, **2**, 337–349.
Schneider, G. (1998). *Ultramicroscopy*, **75**, 85–104.
Varshney, D., Ahmadi, M., Guinel, M. J.-F., Weiner, B. R. & Morell, G. (2012). *Nanoscale Res. Lett.* **7**, 535.
Wasserman, S. R., Whitesides, G. M., Tidswell, I. M., Ocko, B. M., Pershan, P. S. & Axe, J. D. (1989). *J. Am. Chem. Soc.* **111**, 5852–5861.
Werner, M., Chott, A., Fabiano, A. & Battifora, H. (2000). *Am. J. Surg. Pathol.* **24**, 1016–1019.